HHS Public Access

Author manuscript

Nat Neurosci. Author manuscript; available in PMC 2019 August 11.

Published in final edited form as:

Nat Neurosci. 2019 March ; 22(3): 413–420. doi:10.1038/s41593-018-0329-4.

Neutrophil adhesion in brain capillaries reduces cortical blood flow and impairs memory function in Alzheimer's disease mouse models

Jean C. Cruz Hernández[1,*], **Oliver Bracko**[1,*], **Calvin J. Kersbergen**[1], **Victorine Muse**[1], **Mohammad Haft-Javaherian**[1], **Maxime Berg**[2], **Laibaik Park**[3], **Lindsay K. Vinarcsik**[1], **Iryna Ivasyk**[1], **Daniel A. Rivera**[1], **Yiming Kang**[1], **Marta Cortes-Canteli**[4,5], **Myriam Peyrounette**[2], **Vincent Doyeux**[2], **Amy Smith**[2], **Joan Zhou**[1], **Gabriel Otte**[1], **Jeffrey D. Beverly**[1], **Elizabeth Davenport**[1], **Yohan Davit**[2], **Charles P. Lin**[6], **Sidney Strickland**[4], **Costantino Iadecola**[3], **Sylvie Lorthois**[1,2], **Nozomi Nishimura**[1,+], and **Chris B. Schaffer**[1,+]

[1]Nancy E. and Peter C. Meinig School of Biomedical Engineering, Cornell University, Ithaca, NY, USA

[2]Institut de Mécanique des Fluides de Toulouse (IMFT), Université de Toulouse, CNRS, INPT, UPS, Toulouse, France

[3]Feil Family Brain and Mind Research Institute, Weill Cornell Medicine, New York, NY, USA

[4]Patricia and John Rosenwald Laboratory for Neurobiology and Genetics, The Rockefeller University, New York, NY, USA

[5]Centro Nacional de Investigaciones Cardiovasculares Carlos III (CNIC), Madrid, Spain

[6]Wellman Center for Photomedicine and Center for Systems Biology, Massachusetts General Hospital, Harvard Medical School, Boston, MA, USA

Abstract

Cerebral blood flow (CBF) reductions in Alzheimer's disease (AD) patients and related mouse models have been recognized for decades, but the underlying mechanisms and resulting consequences on AD pathogenesis remain poorly understood. In APP/PS1 and 5xFAD mice we found that an increased number of cortical capillaries had stalled blood flow as compared to wildtype animals, largely due to neutrophils that adhered in capillary segments and blocked blood

[+]Corresponding author : nn62@cornell.edu and cs385@cornell.edu.
[*]These authors contributed equally
[+]These authors jointly guided the research

Author Contributions:

JCCH, OB, SL, NN, and CBS conceived the study. JCCH, OB, and CJK performed the *in vivo* imaging experiments. MH, GO and YK developed custom software for data analysis. MH developed custom machine learning algorithms for image segmentation. OB conducted the behavioral studies. LP and CI conducted the ALS-MRI experiments. DR conducted laser speckle imaging studies. MB, MP, VD, AS, YD and SL performed the blood flow simulations. MCC and SS did the stall analyses in the TgCNRD8 mouse model. JCCH, OB, CJK, VM, LKV, II, YK, JZ, JDB, and ED contributed to the analysis of *in vivo* imaging experiments. JCCH, OB, NN and CBS wrote the paper with contributions from MH, MCC, LP, CL, CI, and SL. All authors edited and commented on the manuscript.

Competing Interests Statement:

The authors declare no competing interests.

flow. Administration of antibodies against the neutrophil marker Ly6G reduced the number of stalled capillaries, leading to an immediate increase in CBF and to rapidly improved performance in spatial and working memory tasks. This study identified a novel cellular mechanism that explains the majority of the CBF reduction seen in two mouse models of AD and demonstrated that improving CBF rapidly improved short-term memory function. Restoring cerebral perfusion by preventing neutrophil adhesion may provide a novel strategy for improving cognition in AD patients.

Introduction

Alzheimer's disease (AD) is the most common form of dementia in the elderly, worldwide. AD is characterized by a rapid and progressive cognitive decline accompanied by several pathological features, such as the accumulation of amyloid-beta (Aβ) plaques in brain tissue and along blood vessels as cerebral amyloid angiopathy, the hyperphosphorylation of tau proteins and formation of neurofibrillary tangles in neurons, increased density and activation of inflammatory cells, and ultimately the death of neurons and other brain cells[1].

Vascular dysfunction is implicated in the pathogenesis of AD. Many of the primary risk factors for AD are associated with compromised vascular structure and function, such as obesity, diabetes, atherosclerosis, and hypertension[2]. Brain blood flow is also severely compromised in AD, with both patients with AD[3-5] and mouse models of AD[6-8], which express mutated genes that encode for amyloid precursor protein (APP), exhibiting cortical cerebral blood flow (cCBF) reductions of ~25% early in disease development. Several mechanisms for this hypoperfusion had been proposed including constriction of brain arterioles[9], loss of vascular density[10], and changes in neural activity patterns and/or in neurovascular coupling[11,12], but a full understanding of the underlying mechanisms for CBF reduction in AD has not emerged.

These large blood flow decreases could contribute to the cognitive symptoms of AD and drive disease progression. Cognitive functions, such as attention, were immediately impaired by CBF reductions of ~20% in healthy humans[13]. When CBF was chronically reduced by ~35% in wildtype (wt) mice, spatial memory deficits were observed, accompanied by pathological changes in the brain including increased inflammation[14]. In addition, impairing blood flow in AD mouse models led to an increase in Aβ deposition, suggesting that blood flow deficits can worsen Aβ pathology[14,15]. These data suggest that the decreased CBF in AD likely contributes to both the cognitive dysfunction and to disease progression.

Because CBF reductions have been a recognized and important aspect of AD, yet have not been well explained, we sought to uncover the cellular basis for these flow reductions in the APP/PS1 and 5xFAD mouse models of APP overexpression.

Results

To investigate cortical hypoperfusion in AD, we used *in vivo* two-photon excited fluorescence (2PEF) microscopy to image the cortical vasculature in APP/PS1 mice[16] (Fig. 1a) and looked for occluded vessels (Fig. 1b). We observed no obstructions in arterioles or

venules, but about 1.8% of capillaries in APP/PS1 mice had stalled blood flow, while age- and sex-matched, wt littermates had 0.4% of capillaries not flowing (Fig. 1c, video S1 and S2). The number of stalled capillaries was elevated by 12 weeks of age in APP/PS1 mice, and remained elevated throughout disease progression (Fig. 1d). Flowing and stalled capillaries (Fig. 1e) had about the same distance distribution relative to the nearest penetrating arteriole (Fig. 1f) or ascending venule (Fig. 1g). The incidence of capillary stalling did not increase with Aβ plaque density (Supplementary Fig. 1a), and was the same in awake and anesthetized animals (video S3 and S4; Supplementary Fig. 1b). Capillary stalling was similarly elevated in 5–6 month old 5xFAD (Supplementary Fig. 2a) and 10–13 month old TgCRND8 mice[17] (Supplementary Fig. 3), two different mouse model of APP overexpression.

Using labeling strategies to distinguish leukocytes, platelets, and RBCs (Fig. 2a), we found the majority of stalled capillary segments in APP/PS1 mice contained a leukocyte, sometimes with and sometimes without one or more RBCs also present in the capillary segment (Fig. 2b). We injected a low dose of fluorescently labeled antibodies against Ly6G, a neutrophil surface marker (0.1 mg/kg animal weight, intravenous), and found that the vast majority of capillary stalls had a labeled cell present (Fig. 2c; 26 of 30 identified capillary stalls across four mice were labeled). Stalled capillaries had a modestly smaller average diameter than flowing capillaries (Fig. 2d), but no difference in the density of nearby Aβ deposits (Fig. 2e). Most plugged capillaries were transiently stalled with a half-life of less than 5 min, while one-third remained stalled for 15 min and 10% began flowing and then re-stalled within 15 min (Fig. 2f; Supplementary Fig. 4). We also observed that some capillary segments alternated between flowing and stalled in repeated imaging sessions over weeks (Fig. 2g). The same capillaries were stalled across multiple imaging sessions about ten times as frequently as predicted by a statistical model that assumed each capillary had an equal probability of being stalled at any time point (Fig. 2h). Taken together, these data suggest that the capillary stalls were caused by leukocytes (likely neutrophils based on the specificity of Ly6G expression[18]) plugging a distinct subset of capillary segments.

We serendipitously found that administration of a much higher dose of fluorescently-labeled antibodies against Ly6G (α-Ly6G; 4 mg/kg animal weight, intraperitoneal) reduced the number of stalled capillaries within 10 min (Fig. 3a and Supplementary Fig. 5). Isotype control (Iso-Ctr) antibodies did not impact capillary stalling. Using flow cytometry (Supplementary Fig. 6a) we found that α-Ly6G administration led to no change in the number of circulating neutrophils at three hours (Supplementary Fig. 6b), but did lead to ~50% depletion by six hours (Supplementary Fig. 6c) and near complete depletion by 24 hours (Supplementary Fig. 6d). Median volumetric blood flow in penetrating arterioles, measured using 2PEF (Fig. 3b) and characterizing blood flow into the cortex, increased by 26% in young (3–4 months) and 32% in aged (11–14 months) APP/PS1 mice one hour after α-Ly6G administration (Fig. 3c). This increase in penetrating arteriole blood flow was due to an increase in RBC speed and not an increase in vessel diameter (Supplementary Fig. 7a and b). Penetrating arterioles with lower baseline flow tended to show larger flow increases (Supplementary Fig. 7c). Iso-Ctr antibodies did not change penetrating arteriole blood flow in APP/PS1 mice, nor did α-Ly6G in wt animals (Fig. 3c). We also used arterial spin labeled MRI (ASL-MRI) to measure cCBF in 7–9-month old animals (Fig 3d). At baseline, average

cCBF in APP/PS1 mice was 17% lower than in wt animals (Fig. 3e). cCBF increased by 13% in APP/PS1 mice at ~5 hr after α-Ly6G administration, recovering about two-thirds of the deficit relative to wt animals, but was unchanged in APP/PS1 mice given Iso-Ctr antibodies or wt mice given α-Ly6G (Fig. 3e). To establish the timeline for these CBF increases, we used multi-exposure laser speckle contrast imaging to quantify changes in CBF over the first three hours after antibody administration in APP/PS1 mice. CBF increased within the first 10 min after α-Ly6G administration and remained elevated over the three hours (Supplementary Fig. 8). Isotype control antibodies did not lead to significant changes in CBF (Supplementary Fig. 8). In 5–6 month old 5xFAD mice we also found that α-Ly6G administration led to a reduction in the number of stalled capillaries (Supplementary Fig. 2a) and an increase in blood flow in cortical penetrating arterioles (Supplementary Fig. 2b-d) within an hour. Thus, administration of α-Ly6G led to a rapid reduction in the number of capillary stalls that was accompanied by a rapid increase in cCBF in APP/PS1 and 5xFAD mice. In contrast, when antibodies against LFA-1 were administered to 11–13 month old APP/PS1 mice, we did not observe a rapid decrease in the number of stalled capillaries. Instead, we found that capillary stalls were reduced and penetrating arteriole blood flow was increased at one day after antibody injection, when circulating leukocytes had been depleted (Supplementary Fig. 9). Across all antibody and control treatments in APP/PS1 mice, penetrating arteriole flows increased (decreased) when the number of stalled capillaries decreased (increased) (Supplementary Fig. 9g).

We next tested whether α-Ly6G administration improves cognitive function in APP/PS1 (Fig. 4a) and 5xFAD mice. In the object replacement (OR) test of spatial short-term memory (Fig. 4b), a single dose of α-Ly6G in ~11-month old APP/PS1 mice improved performance to the level of wt animals at 3 and 24 hours after administration (Fig. 4c; Supplementary Fig. 10a). APP/PS1 mice treated with Iso-Ctr antibodies showed no change, nor did wt animals with α-Ly6G (Fig. 4c). In ~6 month old 5xFAD mice, a single dose of α-Ly6G improved animal performance in the OR task at 24 hours, with this trend evident at 3 hours (Supplementary Fig. 11a and b). Similarly, α-Ly6G improved performance of APP/PS1 and 5xFAD mice in the Y-maze test of working memory (Fig. 4d, Supplementary Fig. 10b, and Supplementary Fig. 11c and d). We detected no improvement in sensory-motor function (balance beam walk, Supplementary Fig. 12a-d) nor in depression- and anxiety-like behavior (forced swim, Supplementary Fig. 12e) in APP/PS1 mice with α-Ly6G. To exclude an antibody specific effect we repeated the OR and Y-maze behavioral tests in another cohort of APP/PS1 mice before and after administration of α-LFA-1 antibodies and found improved performance on both tests at 24 hours (Supplementary Fig. 13a-d).

We continued to treat the APP/PS1 mice that received α-Ly6G with additional doses of α-Ly6G every three days for a month, resulting in depletion of neutrophils (Supplementary Fig. 6e). After this regimen, APP/PS1 mice exhibited short-term memory performance that matched wt animals in OR (Fig. 4c), Y-maze (Fig. 4d), and novel object recognition (NOR) (Fig. 4e; Supplementary Fig. 10c and d). We saw no improvement in sensory-motor function (Supplementary Fig. 12a-d) nor in depression- and anxiety-like behavior (Supplementary Fig. 12e).

Because one of the clearance pathways for Aβ is through the vasculature[19] we assessed whether improving cCBF with α-Ly6G decreases the concentration of Aβ monomers and aggregates. Using enzyme-linked immunosorbent assays (ELISAs) of brain extracts from the animals that received one month of antibody treatment, we found that α-Ly6G reduced the concentration of $Aβ_{1–40}$ compared to Iso-Ctr antibodies (Fig. 5a), while the concentration of $Aβ_{1–42}$ (Fig. 5b) and aggregates of Aβ (Supplementary Fig. 14d) remained unchanged. We saw no difference in the number and density of Aβ plaques between α-Ly6G and Iso-Ctr treated animals (Supplementary Fig. 14a – c).

Finally, we addressed the question of how only ~2% of capillaries being stalled could explain the dramatic blood flow changes we observed after α-Ly6G administration. Because each occluded capillary decreases blood flow in up- and down-stream vessels[20], a small number of stalled capillaries could have an outsized impact on CBF. To estimate the magnitude of this impact and to compare how the topology of the cortical capillary network influences the result, we simulated blood flow in vascular networks from a 1 mm^3 volume of mouse parietal cortex (Fig. 6a)[21], a 6 mm^3 volume of human cortex (Fig. 6b)[22], and a synthetic periodic network of order three (Supplementary Fig. 15a) using a non-linear model of microvascular blood flow[23] (see Supplementary Methods and Supplementary Note). cCBF decreased linearly with an increasing fraction of stalled capillaries, without any threshold effect, across all three networks (Fig. 6c), demonstrating that, on average, each single capillary occlusion has a similar, and cumulative, impact on blood flow. Moreover, the slope of the CBF decrease with increasing capillary stalls was almost identical between the mouse, human, and artificial networks, suggesting that capillary stalling may impact CBF similarly across three-dimensional capillary networks with three vessels connected at each node. Quantitatively, these simulations predicted a ~5% (10%) deficit in cCBF due to 2% (4%) of capillaries stalled (relative to the case with no capillary stalls), which is smaller than the increase in CBF we observed with 2PEF and ASL-MRI measurements after α-Ly6G administration.

Discussion

In this study, we aimed to uncover the cellular mechanisms contributing to reduced cCBF in AD and to determine the impact of this reduced cCBF on cognitive function. Brain blood flow reductions occur in the vast majority of dementia patients, including those with AD. These blood flow reductions are one of the earliest features of AD progression[3,24]. Mouse models that express mutant APP also show comparable reductions in CBF[6-8].

Previous studies have implicated a variety of potential mechanisms in the CBF reductions seen in AD. Amyloid beta monomers were found to drive vasoconstriction in brain arterioles that could contribute to a reduction in resting CBF[9]. In AD, there is a faster loss of vascular density with age, which could reduce cerebral perfusion[10]. In addition to decreases in baseline perfusion, the regulation of blood flow in the brain is compromised in AD. Vessel diameter changes in response to CO_2 inhalation, blood pressure changes, and changes in local neural activity are all attenuated in AD patients and mouse models of APP overexpression[25]. This loss of dynamic regulation of cerebral blood flow could also contribute to cognitive impacts. Indeed, recent work showed that restoring cerebrovascular

function, by angiotensin receptor inhibition or by reducing vascular oxidative stress, led to improved cognitive function[12,26,27].

Our data reveal that neutrophil plugging of individual capillary segments is a previously unrecognized mechanism that significantly contributes to the CBF reduction in AD mouse models. The rapid resolution of the capillary stalls after α-Ly6G treatment suggests the stalls are caused by receptor-mediated interactions of neutrophils with the capillary endothelium[28], likely due to increased endothelial inflammation. Ly6G has long been appreciated as a neutrophil-specific marker[29]. Consistent with our findings, it has recently been shown that inhibiting Ly6G signaling leads to decreased migration of neutrophils toward sites of inflammation by modulating β2-integrin-dependent adhesion[28]. There may, however, be other mechanisms that contribute to the reduction in capillary stalling after α-Ly6G treatment. We observed that stalled capillaries had a modestly smaller diameter, on average, than flowing capillaries and a receptor-mediated increase in the mechanical stiffness of neutrophils that was blocked by α-Ly6G might allow for easier deformation and passage of neutrophils through the narrowed capillaries[30]. While some mouse models of AD have shown severe alterations in the topology of the cortical vascular network, recent work has shown that there are relatively minor differences in the capillary density and tortuosity between APP/PS1 and wt mice, suggesting differences in vascular structure likely do not underlie the increase in capillary stalling in APP/PS1 mice[31,32].

Capillary obstructions due to tissue inflammation have been observed in a variety of organ systems (typically at higher incidence than observed here) and have been shown to contribute to the pathology and disease development[33-39]. Inflammation is a persistent and well-recognized feature of AD and previous work has demonstrated an increase in inflammatory adhesion receptors on endothelial cells[40–42], which likely underlies the capillary stalling we observed. A significant contributor to this inflammation is increased reactive oxygen species (ROS) induced by brain exposure to Aβ oligomeric aggregates[26]. These ROS cause a loss of cerebrovascular flow regulation and likely drive the expression of leucocyte-binding receptors on the endothelial cell surface, such as ICAM1 and VCAM1. Our observation that some capillary segments were more likely to stall suggests that the underlying vascular inflammation may not be uniform.

While here our focus has been on increased leukocyte adherence causing a subset of capillaries to be transiently stalled due to a firmly adhered leukocyte, this increased leukocyte adherence likely also contributes to slowed, but not stalled, flow in other capillary segments when a leukocyte is present. Our experimental approach does not enable us to readily detect such slowed vessels. Our simulations included only the impact of completely stalled vessels, which may have contributed to the model's underestimation of the increase in CBF after α-Ly6G administration. However, the simulations predicted a similar sensitivity of brain blood flow to capillary stalling in humans and mice, suggesting that, if capillary stalling occurs in AD patients, significant blood flow improvements could be achieved.

We observed spatial and working memory improvements within 24 hours after treatment with antibodies against Ly6G and/or LFA-1 in multiple mouse models of AD. The temporal

correlation between reduced capillary stalling/blood flow increase and the improvement in cognitive function suggests that a mismatch between neuronal energy metabolism and delivery of energy substrates through blood flow contributes to the cognitive deficit in these AD mouse models.

We also observed improved cognitive function after one month of treatment with α-Ly6G, which depletes neutrophils, in APP/PS1 mice, measured during the antibody therapy. Because of the persistent depletion of neutrophils during this treatment, we expect that capillary stalling was reduced and brain blood flow increased throughout the month, including during cognitive testing, which likely contributed to the improved cognitive performance. In previous work by Zenaro, et al., treatment with antibodies that deplete neutrophils (α-GR-1, α-LFA-1, and α-Ly6G) for one month in multiple AD mouse models (3xTg and 5xFAD), remarkably, led to a persistent improvement in cognitive performance, measured a month after the end of antibody therapy[42]. This persistent improvement in cognitive function was attributed to a decrease in the number of neutrophils present in the brain parenchyma due to their antibody-mediated depletion and a resulting decrease in neuroinflammation, and it is likely this mechanism contributed to the improvement in cognitive performance we observed after one month of antibody therapy. Taken together, these studies show that neutrophil interactions in the vasculature and parenchyma of the brain play a crucial role in the impaired cognitive function observed in multiple mouse models of amyloid-beta overexpression.

Without a firm understanding of the underlying mechanisms that caused reduced CBF in AD, no medical approach to increasing brain blood flow has been developed or tested in humans. In a limited series of experiments in severe AD patients, a piece of omentum, which is known to secrete angiogenic factors and encourage new vessel growth, was surgically placed on the surface of the brain. In the patients that showed an increased CBF as a result, there were signs of improved cognitive function[5,43] Accordingly, improving CBF by interfering with neutrophil adhesion could be a promising therapeutic approach for AD.

Methods

Animals and surgical preparation

All animal procedures were approved by the Cornell Institutional Animal Care and Use Committee (protocol numbers: 2009–0043 and 2015–0029) and were performed under the guidance of the Cornell Center for Animal Resources and Education. We used adult transgenic mice as mouse models of AD, including the APP/PS1 line (B6.Cg-Tg (APPswe, PSEN1dE9) 85Dbo/J; MMRRC_034832-JAX, The Jackson Laboratory)[45] and the 5xFAD line (B6SJL-Tg(APPSwFlLon,PSEN1 *M146L*L286V)6799Vas/Mmjax; MMRRC Stock No: 34840-JAX, The Jackson Laboratory)[46]. Littermate wild-type mice (C57BL/6) were used as controls. Animals were of both sexes and ranged in age from 12 to 100 weeks.

For cranial window implantation, mice were anesthetized under 3% isoflurane on a custom-built stereotactic surgery frame and then maintained on ~1.5% isoflurane in 100% oxygen. Once unresponsive to a toe pinch, mice were given 0.05 mg per 100 g of mouse weight of glycopyrrolate (Baxter Inc.) or 0.005 mg/100 g of atropine (54925–063-10, Med-Pharmex

Inc.) to prevent lung secretions, 0.025 mg/100 g of dexamethasone (07–808-8194, Phoenix Pharm Inc.) to reduce post-surgical inflammation, and 0.5 mg/100 g of ketoprofen (Zoetis Inc.) to reduce post-surgical inflammation and provide post-surgical analgesia. Glycopyrrolate and ketoprofen were injected intramuscularly, while atropine and dexamethasone were injected subcutaneously. Bupivacaine (0.1 ml, 0.125%) (Hospira Inc.) was subcutaneously administered at the incision site to provide a local nerve block. Animals were provided 1 ml per 100 g of mouse weight of 5% (w/v) glucose in normal saline subcutaneously every hour during the procedure. We used a thermometer and feedback-controlled heating blanket (40–90-8D DC, FHC) to maintain body temperature at 37 °C. The head was shaved and washed 3 times with alternating 70% (v/v) ethanol and iodine solutions (AgriLabs). A 6-mm diameter craniotomy was performed over the cerebral cortex using a high-speed drill (HP4–917-21, Fordom) using bits with diameters of 1.4, 0.9, 0.7, and 0.5 mm (Fine Science Tools) for different steps in the craniotomy procedure. The craniotomy was then covered with a sterile 8-mm diameter glass coverslip (11986309, Thermo Scientific), glued onto the remaining skull with cyanoacrylate adhesive (Loctite) and dental cement (Co-Oral-Ite Dental). All procedures were done using sterile technique.

Once the craniotomy was completed, mice were returned to their cages and given injections of 0.025 mg/100 g of dexamethasone and 0.5 mg/100 g of ketoprofen subcutaneously 1 and 2 days after surgery, and all cages were placed over a heating pad during this period. Animals were given at least two weeks to recover from cranial window implantation before experimentation to minimize inflammation from the surgical procedure. Animals were excluded from further study if the clarity of the imaging window was insufficient for 2PEF imaging.

In vivo two-photon microscopy

During imaging sessions, mice were anesthetized with 3% isoflurane, placed on a custom stereotactic frame, and were given glycopyrrolate or atropine and glucose as described above. During imaging, anesthesia was maintained with ~1.5% isoflurane in 100% oxygen, with small adjustments to the isoflurane made to maintain the respiratory rate at ~1 Hz. The mouse was kept at 37 °C with a feedback-controlled heating pad.

To fluorescently label the microvasculature, Texas Red dextran (40 μl, 2.5%, MW = 70,000 kDA, Thermo Fisher Scientific) in saline was injected retro-orbitally immediately prior to imaging. In some animals, amyloid beta (Aβ) deposits were labeled using methoxy-X04[47]. In early experiments using methoxy-X04 obtained directly from Prof. Klunk at the University of Pittsburgh, we retro-orbitally injected 40 μL of 1 mg/ml methoxy-X04 in 0.9% saline (adjusted to pH 12 with 0.1 N NaOH) immediately prior to imaging. In later experiments using methoxy-X04 available commercially from Tocris, we intraperitoneally injected methoxy-X04 (dissolved in DMSO at 100 mM) one day prior to imaging at a dose of 1 mg/100 g. We observed no obvious differences in the amyloid labeling between these two administration approaches. In some animals, leukocytes and blood platelets were labeled with a retro-orbital injection of Rhodamine 6G (0.1 ml, 1 mg/ml in 0.9% saline, Acros Organics, Pure)[38]. Leukocytes were distinguished from blood platelets with a retro-orbital injection of Hoechst 33342 (50 μl, 4.8 mg/ml in 0.9% saline, Thermo Fisher

Scientific). Texas Red (and methoxy-X04, when given retro-orbitally) were dosed in a single syringe, while Rhodamine 6G and Hoechst were dosed together in a second syringe.

Three-dimensional images of the cortical vasculature and measurement of red blood cell flow speeds in specific vessels were obtained via a custom-built two-photon excited fluorescence (2PEF) microscope. Imaging was done using 830-nm, 75-fs pulses from a Ti:Sapphire laser oscillator (MIRA HP pumped by a Verdi-V18 or Vision S, Coherent) and 900-nm, 75-fs pulses from a second Ti:Sapphire laser oscillator (Vision S, Coherent). Lasers were scanned by galvonometric scanners (1 frame/s) and focused into the sample using a 20× water-immersion objective lens for high-resolution imaging (numerical aperture (NA) = 1.0, Carl Zeiss Microscopy; or NA = 0.95, Olympus), or a 4× objective for mapping of the cortical surface vasculature (NA = 0.28, Olympus). The emitted fluorescence was detected on either a two-channel detection system or, for later data sets, on an upgraded four-channel detection system. On the two-channel system, the fluorescence was split by a 600-nm long pass dichroic and two successive image stacks were acquired first with 645/45 nm (center wavelength/bandwidth) and 575/25 nm bandpass filters to image Texas Red and Rhodamine 6G, respectively, and then with 645/65 nm and 460/50 nm filters to image Texas Red and both methoxy-X04 and Hoescht (on the same channel), all under 830-nm excitation. On the four-channel system, a secondary long-pass dichroic at 520 nm was followed by tertiary long-pass dichroics at 458 nm and one at either 562 or 605 nm. Emission was detected on four photomultiplier tubes through the following emission filters: 417/60 nm for Hoechst, 494/41 nm for methoxy-X04, 550/49 nm for Rhodamine 6G, and 641/75 nm for Texas Red. Laser excitation was 830 nm except when trying to image deep cortical tissue in animals where only Texas Red was present in which case 900-nm excitation was used. Laser scanning and data acquisition was controlled by ScanImage software[48]. To visualize the cortical vasculature, stacks of images spaced by 1 μm axially were taken to a cortical depth of 300–500 μm.

For imaging of neutrophils labeled with anti-Ly6G antibodies labeled with Alexa488, imaging was performed on a custom-built 2PEF microscope at the Wellman Center for Photomedicine. In these animals, neutrophils were labeled with a tail vein injection of anti-Ly6G-Alexa 488 (0.1 mg/kg animal weight, 127626-Biolegend) at the same time as the labeling of blood plasma with Texas Red dextran. Imaging was done using 750-nm, 80-fs pulses from a Ti:Sapphire laser oscillator (Spectra-Physics Mai Tai). The laser beam was scanned by polygon scanners (30 frames/s) and focused into the sample using a 40x water-immersion objective lens for high-resolution imaging (NA = 0.80, Olympus), or a 10x objective for mapping of the cortical surface vasculature (NA = 0.30, Olympus). The emitted fluorescence was detected on photomultiplier tubes through the following emission filters: 525/50 nm for Alexa-488 and 605/50 nm for Texas Red. Laser scanning and data acquisition was controlled by custom built software. Stacks of images spaced by 1 μm axially were taken to a cortical depth of 100–200 μm.

Quantification of capillary network topology and capillary segment stalling

The 2PEF images of vascular networks were manually traced in three-dimensions to create a vectorized skeleton that represents the cortical vasculature using custom-written tracing

software. The researchers producing these tracings were blinded to the genotype of the animal and any treatment it had received. Volumes of these image stacks where vessels could not be readily identified and traced were excluded from all analysis. These regions were typically deep and near the edges of the imaged volume, or occasionally directly underneath a large surface vessel. Vessel segments were classified as surface and penetrating arterioles, capillaries, or ascending and surface venules. All vessels smaller than 10 μm in diameter were classed as capillaries. Large surface arterioles were distinguished from large surface venules based on morphology (arterioles were smaller diameter, had smoother walls and less tortuosity, and tended to branch more symmetrically and in Y-shape junctions as compared to venules). Other arterioles or venules were classed by tracing their connectivity to these readily identifiable large vessels.

Each capillary segment in these images was then manually classed as either flowing or stalled based on the motion of RBCs during the entire time each capillary was visible in the 3D image stack. The Texas Red dextran labels the blood plasma, but not the blood cells, so RBCs and other blood cells show up as dark patches in the vessel lumen. The motion of these dark patches indicates flowing blood cells. Each capillary segment was visible in a minimum of ~5 successive frames in the 3D image stack, or for ~5 s (capillaries not oriented parallel to the cortical surface were observed for significantly more frames). We scored a capillary segment as stalled if we did not see motion of the RBCs and other cells in the capillary segment over this observation time. This manual scoring of capillaries as flowing or stalled was performed with the researcher blinded to the genotype and treatment status of the animal. In addition, this scoring was performed using only the image data visible on the Texas Red imaging channel. All animals included in our analysis had at least 800 capillary segments scored as flowing or stalled. Animals with fewer characterized capillaries were excluded.

Using the traced vascular network, the topologically shortest path from each flowing or stalled capillary to the nearest penetrating arteriole and ascending venule was calculated using Dijkstra's algorithm[49].

Distinguishing causes of capillary stalls

In some animals, once capillary stalls were identified we used the additional fluorescent labels to determine what was blocking blood flow in the capillary segment. Stalled capillary segments with a cell-shaped object labeled with both Rhodamine 6G and Hoechst present were scored as having a leukocyte. Stalled segments with punctate objects labeled with Rhodamine 6G alone were scored as having platelet aggregates. Stalled capillary segments with only RBCs present were classed as RBC stalls. We determined what fraction of stalled capillaries had only a leukocyte, a leukocyte with one or more RBCs present, only platelet aggregates, platelet aggregates with RBCs, and only RBCs. With this labeling scheme, we were unable to reliably distinguish platelet aggregates when a leukocyte was present. Additional experiments used a low-dose of Alexa 488 labeled anti-Ly6G antibodies to assess the type of leukocyte associated with capillary stalls.

We assessed if the diameter of flowing and stalled capillaries was different, on average. First, image stacks were linearly interpolated to have an isotropic 1 μm voxel size. To reduce

the salt and pepper noise in the vascular images, we filtered using a 3D 5 × 5 × 5 pixel Gaussian filter. We then corrected for unevenness in the image intensity by filtering the image (85 × 85 pixel sized mean filter) and subtracting this from the Gaussian filtered image. The resulting image was binarized using Otsu's method[50]. Finally, objects smaller than 1000 voxels were eliminated, where voxels were considered part of the same connected object whenever they shared at least a corner. We then used this binarized image to correct the manual tracing of the vasculature by shifting the centerline so it was equidistant from the vessel boundaries (done within a 10-μm neighborhood to avoid confusion between neighboring capillaries). Every 5 μm along the centerline of each capillary segment, we estimated the vessel radius by finding the closest distance from the centerline to the vessel boundary. Measurements of less than 2 μm or more than 10 μm were excluded as they likely reflected imaging artifacts, and we averaged across all measurements for each capillary segment.

Administration of antibodies against Ly6G or LFA-1 to interfere with capillary stalling

We treated APP/PS1 and 5xFAD mice with intraperitoneal injections of monoclonal antibodies against lymphocyte antigen 6 complex, locus G (Ly6G) (α-Ly6G, clone 1A8, 4 mg/kg, BD Biosciences) or an isotype control antibody (Rat IgG2a, κ, 4 mg/kg, BD Biosciences). In addition, APP/PS1 mice were treated with retroorbital or intraperitoneal injections of monoclonal antibodies against Lymphocyte Functional Antigen 1 (α-LFA-1; M17/4 clone, BD Biosciences; 4 mg/kg). The same cortical capillary bed was imaged in anesthetized mice immediately before and at 60–90 min after treatment. Mice were randomly assigned to receive treatment or isotype control antibodies and the experimenter was blinded to both mouse genotype and whether the antibody was the treatment or control during the experiment. Quantification of stalled capillaries was performed by researchers blinded to imaging time, animal genotype, and treatment type.

Behavior Experiments

All experiments were performed under red light in an isolated room. The position of the mouse's nose was automatically traced by Viewer III software (Biobserve, Bonn, Germany). In addition to the automatic results obtained by Viewer III software, a blinded experimenter independently scored mouse behavior manually. Animals were taken into the behavior room one-hour prior to the experiment. Behavioral analysis was conducted at baseline and at 3 and 24 h after injection with α-Ly6G, α-LFA-1, or isotype control antibodies (IP 4 mg/kg). The α-Ly6G treated APP/PS1 mice were then treated every three days for four weeks (IP 2 mg/kg) and behavior experiments were repeated. The OR, Y-maze, balance beam walk, and forced swim tests were performed at all time points. The NOR task was performed only at baseline and the 4-week time point to avoid animals becoming accustomed to the objects. For experiments with APP/PS1 mice and α-Ly6G, animals were ~11 months of age at the start of the experiment. For experiments with APP/PS1 mice and α-LFA-1, animals were 11–13 months of age. For experiments with 5xFAD mice and α-Ly6G, animals were 5–6 months of age. Mice were randomly assigned to receive treatment or isotype control antibodies and the experimenter was blinded to both mouse genotype and whether the antibody was the treatment or control during the experiment.

Object replacement test: The object replacement (OR) task evaluated spatial memory performance. All objects used were first validated in a separate cohort of mice to ensure that no intrinsic preference or aversion was observed and animals explored all objects similarly. Exploration time for the objects was defined as any time when there was physical contact with an object (whisking, sniffing, rearing on, or touching the object) or when the animal was oriented toward the object and the head was within 2 cm of the object. In trial 1, mice were allowed to explore two identical objects for 10 min in the arena and then returned to their home cage for 60 min. Mice were then returned to the testing arena for 3 min with one object moved to a novel location (trial 2). Care was taken to ensure that the change of placement alters both the intrinsic relationship between objects (e.g. a rotation of the moved object) and the position relative to internal visual cues (e.g. new location in the arena; one wall of testing arena had a pattern). At subsequent time points, new object positions and new pairs of objects (from the validated pool of objects) were used to maintain animal interest. In addition to using the tracking software to determine the object exploration times, the time spent at each object was manually scored by an independent experimenter who was blinded to the genotype and treatment. The preference score (%) for OR tasks was calculated as ([exploration time of the novel object]/[exploration time of both objects]) × 100 from the data in trial 2. Automated tracking and manual scoring yielded similar results across groups, so we report the automated tracking results.

Y-Maze: The Y-Maze task was used to measure working memory by quantifying spontaneous alternation between arms of the maze. The Y-maze consisted of three arms at 120° and was made of light grey plastic. Each arm was 6-cm wide and 36-cm long, and had 12.5-cm high walls. The maze was cleaned with 70% ethanol after each mouse. A mouse was placed in the Y-maze and allowed to explore for 6 min. Mouse behavior was monitored, recorded, and analyzed using the Viewer software. A mouse was considered to have entered an arm if the whole body (except for the tail) entered the arm and to have exited if the whole body (except for the tail) exited the arm. If an animal consecutively entered three different arms, it was counted as an alternating trial. Because the maximum number of triads is the total number of arm entries minus 2, the spontaneous alternation score was calculated as (number of alternating triads)/(total number of arm entries − 2).

Novel object recognition test: The novel object recognition (NOR) task measures recognition memory and is based on rodents' innate preference for exploring novel objects. This test was conducted only in the animals at baseline and after 4 weeks of treatment. The testing approach was identical to the OR task, but with a novel object placed at the location of one of the initial objects in trial 2. To exclude preference bias for particular objects in the first trial one animal would see two of object A and another animal two of object B. In the second trial to test for preference for a novel object, both animals see one of object A and one of object B. For the repeat of the test at 4 weeks, we used new objects C and D.

ELISA Assay

After the conclusion of the behavior experiments, the APP/PS1 animals that had received α-Ly6G or isotype control antibodies every 3 days for a month were sacrificed by lethal injection of pentobarbital (5 mg/100 g). Brains were quickly extracted and divided along the

centerline. One half was immersed in 4% paraformaldehyde in phosphate buffered saline (PBS) for later histological analysis and the other half was snap frozen in liquid nitrogen.

The frozen APP/PS1 mouse hemi-brains (Iso-Ctr: n=6, 11.5–12.5 months old; α-Ly6G: n=7, 11.5–12.5 months old) were weighed and homogenized in 1 ml PBS containing complete protease inhibitor (Roche Applied Science) and 1 mM AEBSF (Sigma) using a Dounce homogenizer. The homogenates were then sonicated and centrifuged at 14,000 g for 30 min at 4° C. The supernatant (PBS-soluble fraction) was removed and stored at −80° C. The pellet was re-dissolved in 0.5 ml 70% formic acid, sonicated, and centrifuged at 14,000 g for 30 min at 4° C, and the supernatant was removed and neutralized using 1M Tris buffer at pH 11. Protein concentration was measured in the PBS soluble fraction and the formic acid soluble fraction using the Pierce BCA Protein Assay (Thermo Fischer Scientific). The PBS soluble fraction extracts were diluted 1:5. Formic acid extracts were diluted 1:1 after neutralization. These brain extracts were analyzed by sandwich ELISA for Aβ1–40, Aβ1–42, and Aβ aggregates using commercial ELISA kits and following the manufacturer's protocol (Aβ1–40: KHB3481; Aβ1–42: KHB3441; Aβ aggregates: KHB3491, Thermo Fisher Scientific). The Aβ concentration was calculated by comparing the sample absorbance with the absorbance of known concentrations of synthetic Aβ1–40 and Aβ1–42 standards on the same plate. Data was acquired with a Synergy HT plate reader (Biotek) and analyzed using Gen5 software (BioTek) and Prism (Graphpad).

Statistical analysis

Boxplots were created using Prism7 (GraphPad). The box extends between the values for the 25th and 75th percentile of the data. The whiskers extend 1.5 times the difference between the value of the 75th and 25th percentile of the data from the top and bottom of the box. Values lying outside the whiskers were defined as outliers and the mean was computed excluding these outliers. The median is indicated with a black horizontal line inside the box, while the mean is indicated with a red horizontal line. Violin plots were created using the statistical software package, R[51].

Data in all groups was tested for normality using D'Agostino-Pearson omnibus normality test. Parametric statistics were used only if the data in all groups in the comparison were normally distributed. The statistical significance of differences between multiple groups was determined using one-way analysis of variance (ANOVA) followed by Tukey's multiple comparison correction for normally distributed data, and using one-way Kruskal-Wallis ANOVA followed by Dunn's multiple comparison correction for data with a non-normal distribution. To compare baseline and post-treatment measurements at multiple time points with non-normal data, the Friedman one-way repeated measures non-parametric ANOVA followed by Dunn's multiple comparison correction was used. Statistical comparisons between two groups were performed using the Student's t test or paired t test for normally distributed data, or using the Mann-Whitney test or Wilcoxon matched-pairs test for data with a non-normal distribution. P-values smaller than 0.05 were considered statistically significant. All statistical analysis was performed using Prism7 (GraphPad).

We use a standardized set of significance indicators across all figures in this manuscript. For comparisons between groups: *p<0.05, **p<0.01, ***p<0.001, ****p<0.0001. For matched

comparisons before and after treatment: +p<0.05, ++p<0.01. Details of the groups compared, animal and capillary numbers, sex distributions, statistical tests, exact p-values, and explanatory notes for individual panels are included in the figure captions.

Additional methodological details

Additional information on the methods used in this study are available in the Supplementary Methods.

Data availability

The raw data reported in this manuscript are archived at https://doi.org/10.7298/9PR3-D773.

Code availability

Code for 3D tracing, vessel segmentation, analysis of linescan data, and determination of amyloid density around capillaries can be obtained by contacting NN or CBS. Code for simulation of blood flow in vascular networks can be obtained by contacting SL.

Supplementary Material

Refer to Web version on PubMed Central for supplementary material.

Acknowledgments

This work was supported by the National Institutes of Health grants AG049952 (CBS), NS37853 (CI), and AG031620 (NN), the Alzheimer's Drug Discovery Foundation (CBS), the Alzheimer's Art Quilt Initiative (CBS), the BrightFocus Foundation (CBS), European Research Council grant 615102 (SL), the DFG German Research Foundation (OB), a National Science Foundation Graduate Research Fellowship (JCH), the L'Oréal Fellowship for Women in Science (NN), and used computing resources at CALMIP (SL). We thank Frédéric Lauwers for the human vascular data, Philibert Tsai, Pablo Blinder and David Kleinfeld for the mouse vascular data, and Maria Gulinello for guidance on behavior experiments. Finally, we thank Joseph R. Fetcho, Jesse H. Goldberg, and Michael I. Kotlikoff for commenting on the manuscript.

References:

1. Wang J, Gu BJ, Masters CL & Wang YJ A systemic view of Alzheimer disease - insights from amyloid-beta metabolism beyond the brain. Nature reviews. Neurology 13, 612–623, doi:10.1038/nrneurol.2017.111 (2017). [PubMed: 28960209]
2. Santos CY et al. Pathophysiologic relationship between Alzheimer's disease, cerebrovascular disease, and cardiovascular risk: A review and synthesis. Alzheimer's & dementia 7, 69–87, doi:10.1016/j.dadm.2017.01.005 (2017).
3. Iturria-Medina Y et al. Early role of vascular dysregulation on late-onset Alzheimer's disease based on multifactorial data-driven analysis. Nature communications 7, 11934, doi:10.1038/ncomms11934 (2016).
4. Dai W et al. Mild cognitive impairment and alzheimer disease: patterns of altered cerebral blood flow at MR imaging. Radiology 250, 856–866, doi:10.1148/radiol.2503080751 (2009). [PubMed: 19164119]
5. Wolters FJ et al. Cerebral Perfusion and the Risk of Dementia: A Population-Based Study. Circulation, doi:10.1161/CIRCULATIONAHA.117.027448 (2017).
6. Wiesmann M et al. Hypertension, cerebrovascular impairment, and cognitive decline in aged AbetaPP/PS1 mice. Theranostics 7, 1277–1289, doi:10.7150/thno.18509 (2017). [PubMed: 28435465]

7. Li H et al. Vascular and parenchymal amyloid pathology in an Alzheimer disease knock-in mouse model: interplay with cerebral blood flow. Molecular neurodegeneration 9, 28, doi: 10.1186/1750-1326-9-28 (2014). [PubMed: 25108425]
8. Niwa K, Kazama K, Younkin SG, Carlson GA & Iadecola C Alterations in cerebral blood flow and glucose utilization in mice overexpressing the amyloid precursor protein. Neurobiology of disease 9, 61–68, doi:10.1006/nbdi.2001.0460 (2002). [PubMed: 11848685]
9. Niwa K et al. A beta-peptides enhance vasoconstriction in cerebral circulation. American journal of physiology. Heart and circulatory physiology 281, H2417–2424 (2001). [PubMed: 11709407]
10. Farkas E & Luiten PG Cerebral microvascular pathology in aging and Alzheimer's disease. Progress in neurobiology 64, 575–611 (2001). [PubMed: 11311463]
11. Chen Y et al. Voxel-level comparison of arterial spin-labeled perfusion MRI and FDG-PET in Alzheimer disease. Neurology 77, 1977–1985, doi:10.1212/WNL.0b013e31823a0ef7 (2011). [PubMed: 22094481]
12. Royea J, Zhang L, Tong XK & Hamel E Angiotensin IV Receptors Mediate the Cognitive and Cerebrovascular Benefits of Losartan in a Mouse Model of Alzheimer's Disease. The Journal of neuroscience : the official journal of the Society for Neuroscience 37, 5562–5573, doi:10.1523/JNEUROSCI.0329-17.2017 (2017). [PubMed: 28476949]
13. Marshall RS et al. Recovery of brain function during induced cerebral hypoperfusion. Brain : a journal of neurology 124, 1208–1217 (2001). [PubMed: 11353736]
14. Wang L et al. Chronic cerebral hypoperfusion induces memory deficits and facilitates Abeta generation in C57BL/6J mice. Experimental neurology 283, 353–364, doi:10.1016/j.expneurol.2016.07.006 (2016). [PubMed: 27421879]
15. Hattori Y et al. Gradual Carotid Artery Stenosis in Mice Closely Replicates Hypoperfusive Vascular Dementia in Humans. Journal of the American Heart Association 5, doi:10.1161/JAHA.115.002757 (2016).
16. Radde R et al. Abeta42-driven cerebral amyloidosis in transgenic mice reveals early and robust pathology. EMBO reports 7, 940–946, doi:10.1038/sj.embor.7400784 (2006). [PubMed: 16906128]
17. Chishti MA et al. Early-onset amyloid deposition and cognitive deficits in transgenic mice expressing a double mutant form of amyloid precursor protein 695. The Journal of biological chemistry 276, 21562–21570, doi:10.1074/jbc.M100710200 (2001). [PubMed: 11279122]
18. Hasenberg A et al. Catchup: a mouse model for imaging-based tracking and modulation of neutrophil granulocytes. Nature methods 12, 445–452, doi:10.1038/nmeth.3322 (2015). [PubMed: 25775045]
19. Deane R, Bell RD, Sagare A & Zlokovic BV Clearance of amyloid-beta peptide across the blood-brain barrier: implication for therapies in Alzheimer's disease. CNS & neurological disorders drug targets 8, 16–30 (2009). [PubMed: 19275634]
20. Nishimura N et al. Targeted insult to subsurface cortical blood vessels using ultrashort laser pulses: three models of stroke. Nature methods 3, 99–108, doi:10.1038/nmeth844 (2006). [PubMed: 16432519]
21. Tsai PS et al. Correlations of neuronal and microvascular densities in murine cortex revealed by direct counting and colocalization of nuclei and vessels. The Journal of neuroscience : the official journal of the Society for Neuroscience 29, 14553–14570, doi:10.1523/JNEUROSCI.3287-09.2009 (2009). [PubMed: 19923289]
22. Lauwers F, Cassot F, Lauwers-Cances V, Puwanarajah P & Duvernoy H Morphometry of the human cerebral cortex microcirculation: general characteristics and space-related profiles. NeuroImage 39, 936–948, doi:10.1016/j.neuroimage.2007.09.024 (2008). [PubMed: 17997329]
23. Lorthois S, Cassot F & Lauwers F Simulation study of brain blood flow regulation by intra-cortical arterioles in an anatomically accurate large human vascular network. Part II: flow variations induced by global or localized modifications of arteriolar diameters. NeuroImage 54, 2840–2853, doi:10.1016/j.neuroimage.2010.10.040 (2011). [PubMed: 21047557]
24. Roher AE et al. Cerebral blood flow in Alzheimer's disease. Vascular health and risk management 8, 599–611, doi:10.2147/VHRM.S34874 (2012). [PubMed: 23109807]

25. Iadecola C The Neurovascular Unit Coming of Age: A Journey through Neurovascular Coupling in Health and Disease. Neuron 96, 17–42, doi:10.1016/j.neuron.2017.07.030 (2017). [PubMed: 28957666]
26. Park L et al. Nox2-derived radicals contribute to neurovascular and behavioral dysfunction in mice overexpressing the amyloid precursor protein. Proceedings of the National Academy of Sciences of the United States of America 105, 1347–1352, doi:10.1073/pnas.0711568105 (2008). [PubMed: 18202172]
27. Park L et al. Innate immunity receptor CD36 promotes cerebral amyloid angiopathy. Proceedings of the National Academy of Sciences of the United States of America 110, 3089–3094, doi: 10.1073/pnas.1300021110 (2013). [PubMed: 23382216]
28. Wang JX et al. Ly6G ligation blocks recruitment of neutrophils via a beta2-integrin-dependent mechanism. Blood 120, 1489–1498, doi:10.1182/blood-2012-01-404046 (2012). [PubMed: 22661700]
29. Daley JM, Thomay AA, Connolly MD, Reichner JS & Albina JE Use of Ly6G-specific monoclonal antibody to deplete neutrophils in mice. Journal of leukocyte biology 83, 64–70, doi: 10.1189/jlb.0407247 (2008). [PubMed: 17884993]
30. Lavkan AH, Astiz ME & Rackow EC Effects of proinflammatory cytokines and bacterial toxins on neutrophil rheologic properties. Critical care medicine 26, 1677–1682 (1998). [PubMed: 9781725]
31. Bennett RE et al. Tau induces blood vessel abnormalities and angiogenesis-related gene expression in P301L transgenic mice and human Alzheimer's disease. Proceedings of the National Academy of Sciences of the United States of America 115, E1289–E1298, doi:10.1073/pnas.1710329115 (2018). [PubMed: 29358399]
32. Mohammad Haft-Javaherian LF, Victorine Muse, Schaffer Chris B., Nozomi Nishimura, Sabuncu Mert R.. Deep convolutional neural networks for segmenting 3D in vivo multiphoton images of vasculature in Alzheimer disease mouse models. arXiv preprint arXiv:1801.00880. (2018).
33. Villringer A et al. Imaging of leukocytes within the rat brain cortex in vivo. Microvascular research 42, 305–315 (1991). [PubMed: 1723482]
34. Ishikawa M et al. Leukocyte plugging and cortical capillary flow after subarachnoid hemorrhage. Acta neurochirurgica 158, 1057–1067, doi:10.1007/s00701-016-2792-6 (2016). [PubMed: 27040552]
35. Kloner RA No-reflow phenomenon: maintaining vascular integrity. Journal of cardiovascular pharmacology and therapeutics 16, 244–250, doi:10.1177/1074248411405990 (2011). [PubMed: 21821523]
36. Engler RL, Schmid-Schonbein GW & Pavelec RS Leukocyte capillary plugging in myocardial ischemia and reperfusion in the dog. The American journal of pathology 111, 98–111 (1983). [PubMed: 6837725]
37. Chibber R, Ben-Mahmud BM, Chibber S & Kohner EM Leukocytes in diabetic retinopathy. Current diabetes reviews 3, 3–14 (2007). [PubMed: 18220651]
38. Santisakultarm TP et al. Stalled cerebral capillary blood flow in mouse models of essential thrombocythemia and polycythemia vera revealed by in vivo two-photon imaging. Journal of thrombosis and haemostasis : JTH 12, 2120–2130, doi:10.1111/jth.12738 (2014). [PubMed: 25263265]
39. Ilesanmi OO Pathological basis of symptoms and crises in sickle cell disorder: implications for counseling and psychotherapy. Hematology reports 2, e2, doi:10.4081/hr.2010.e2 (2010). [PubMed: 22184515]
40. Zuliani G et al. Markers of endothelial dysfunction in older subjects with late onset Alzheimer's disease or vascular dementia. Journal of the neurological sciences 272, 164–170, doi:10.1016/j.jns. 2008.05.020 (2008). [PubMed: 18597785]
41. Iadecola C Vascular and Metabolic Factors in Alzheimer's Disease and Related Dementias: Introduction. Cellular and molecular neurobiology 36, 151–154, doi:10.1007/s10571-015-0319-y (2016). [PubMed: 26898551]
42. Zenaro E et al. Neutrophils promote Alzheimer's disease-like pathology and cognitive decline via LFA-1 integrin. Nature medicine 21, 880–886, doi:10.1038/nm.3913 (2015).

43. Goldsmith HS Alzheimer's disease can be treated: Why the delay? Surgical neurology international 8, 133, doi:10.4103/sni.sni_116_17 (2017). [PubMed: 28781910]

44. Blinder P et al. The cortical angiome: an interconnected vascular network with noncolumnar patterns of blood flow. Nature neuroscience 16, 889–897, doi:10.1038/nn.3426 (2013). [PubMed: 23749145]

Methods-only References:

45. Jankowsky JL et al. Mutant presenilins specifically elevate the levels of the 42 residue beta-amyloid peptide in vivo: evidence for augmentation of a 42-specific gamma secretase. Hum Mol Genet 13, 159–170, doi:10.1093/hmg/ddh019 (2004). [PubMed: 14645205]

46. Oakley H et al. Intraneuronal beta-amyloid aggregates, neurodegeneration, and neuron loss in transgenic mice with five familial Alzheimer's disease mutations: potential factors in amyloid plaque formation. The Journal of neuroscience : the official journal of the Society for Neuroscience 26, 10129–10140, doi:10.1523/JNEUROSCI.1202-06.2006 (2006). [PubMed: 17021169]

47. Klunk WE et al. Imaging Abeta plaques in living transgenic mice with multiphoton microscopy and methoxy-X04, a systemically administered Congo red derivative. J Neuropathol Exp Neurol 61, 797–805 (2002). [PubMed: 12230326]

48. Pologruto TA, Sabatini BL & Svoboda K ScanImage: flexible software for operating laser scanning microscopes. Biomed Eng Online 2, 13, doi:10.1186/1475-925X-2-13 (2003). [PubMed: 12801419]

49. Dijkstra EW A note on two problems in connexion with graphs. Numerische Mathematik Volume 1, 269–271, doi:10.1007/BF01386390 (1959).

50. Otsu N A threshold selection method from gray-level histogram. IEEE Trans. Syst. Man Cybern 9, 62–66, doi:10.1109/TSMC.1979.4310076 (1979).

51. Team RCR: A language and environment for statistical computing. Foundation for Statistical Computing (2013).

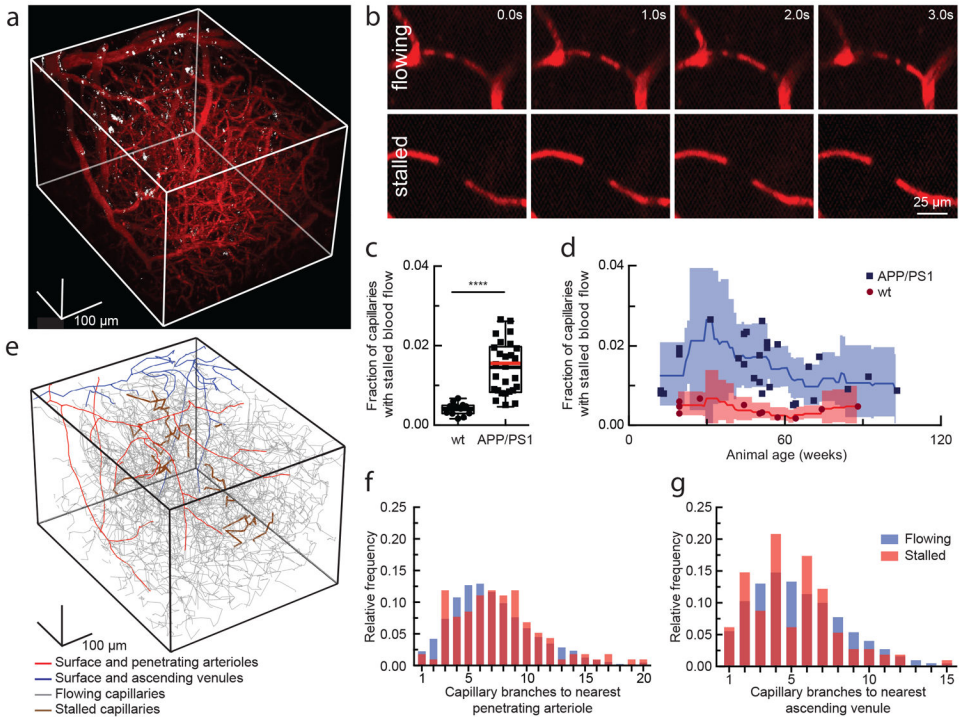

Fig. 1. 2PEF imaging of mouse cortical vasculature revealed a higher fraction of plugged capillaries in APP/PS1 mice.

(a) Rendering of 2PEF image stack of cortical vasculature (red; Texas Red dextran) and amyloid deposits (white; methoxy-X04). (b) Individual brain capillaries were scored as flowing or stalled based on the motion of unlabeled blood cells (black) within the fluorescently labeled blood plasma (red). (c) Fraction of capillaries with stalled blood flow in APP/PS1 and wt mice. (APP/PS1: n = 28 mice (7 female, 21 male), ~22,400 capillaries, and wt: n = 12 mice (10 female, 2 male), ~9,600 capillaries; Two-tailed Mann-Whitney, $p=6.8 \times 10^{-9}$; Boxplot: whiskers extend 1.5 times the difference between the value of the 75th and 25th percentile, median=black line and mean= red line.) (d) same data in c shown as a function of animal age. Each data point represents the fraction of capillaries stalled in one mouse, with a minimum of 800 capillaries scored per mouse. Curves represent sliding averages with a 10-week window and shaded areas represent 95% confidence intervals. Data from one outlier mouse not shown in c and d: APP/PS1, 42 weeks, 4.4% stalled. (e) Tracing of the vascular network in panel a, with stalled capillaries indicated in brown. (f) and (g) Histograms showing the topological location of flowing and stalled capillaries in APP/PS1 mice relative to the nearest penetrating arteriole and ascending venule, respectively (n = 8 mice (5 female, 3 male), 120 stalled and ~8,700 flowing capillaries).

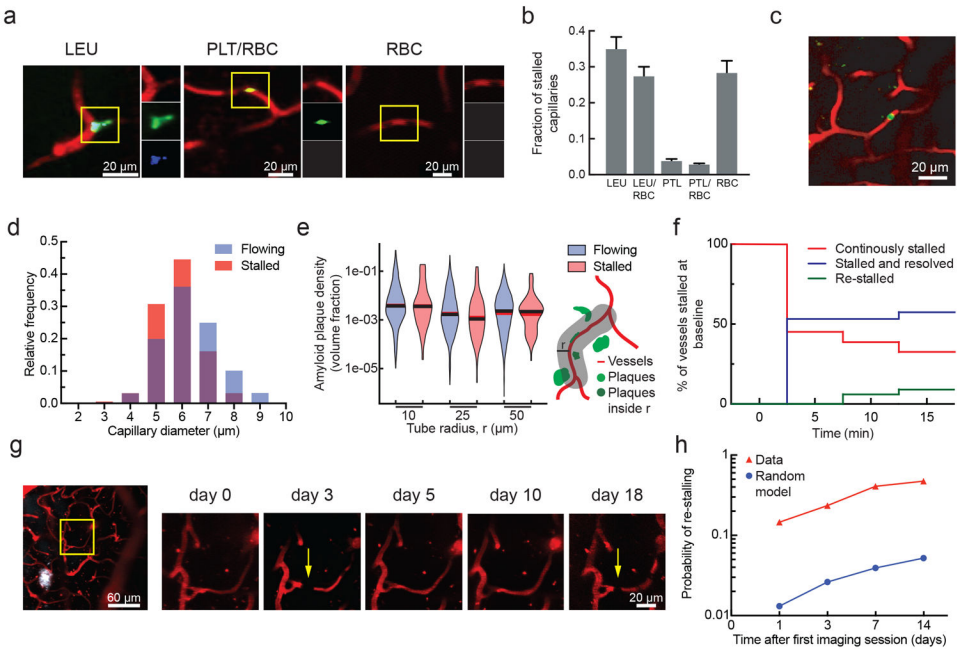

Fig. 2. Characterization of the cause, location, and dynamics of capillary occlusions in APP/PS1 mice.

(a) 2PEF images of stalled capillaries that contained a leukocyte (LEU, left), platelet aggregates (PLT) and RBCs (center), or only RBCs (right), distinguished by fluorescent labels (red: Texas Red-labeled blood plasma; green: rhodamine 6G-labeled leukocytes and platelets; blue: Hoechst-labeled leukocyte nuclei). (b) Fraction of stalled capillaries in APP/PS1 mice that contained LEU, one or more RBCs, and PLT, distinguishing cases of LEU only, LEU with one or more RBCs, PLT only, PLT with RBCs, and RBCs only (n = 6 mice (3 female, 3 male) and 106 stalls; error bars represent 95% confidence intervals based on binomial statistics.) (c) Projection of 2PEF image stack showing an anti-Ly6G labeled cell in a stalled capillary (red: Texas Red-labeled blood plasma; green: anti-Ly6G-Alexa 488 (0.1 mg/kg animal weight, intravenous). (d) Histogram of the diameter of flowing and stalled capillaries in APP/PS1 mice (Averages: 5.8±0.84 µm (stalled), 6.3±1.1 µm (flowing) (mean±SD); Two-tailed Mann-Whitney, p=0.000020; n = 7 mice (4 female, 3 male), 116 stalled and ~8,400 flowing capillaries). (e) Violin plot of the density of amyloid deposits within tubes of different radii that followed the capillary centerline for flowing and stalled capillary segments in APP/PS1 mice (n = 7 mice (4 female, 3 male), 116 stalled and ~8,400 flowing capillaries). The vertical range of the violin plot represents the full range of measured values, while the width of the violin indicates the frequency of those values. The red (black) horizontal line indicates the mean (median) value. (f) Fraction of stalled capillaries that remained stalled (red), resumed flowing (green), or resumed flowing and then re-stalled (blue) over 15 minutes in APP/PS1 mice (n = 3 mice (all male), 31 capillary segments). (g) 2PEF images of the same capillary alternately stalled (arrows) and flowing over several weeks (white: methoxy-X04). (h) Probability of an initially stalled capillary to be observed stalled again at any subsequent imaging time point, showing both real observations in APP/PS1 mice and predictions from a model that assumed each capillary

had an equal probability of stalling at each time point (n=4 mice (2 female, 2 male), 49 stalled capillaries followed from the first imaging session).

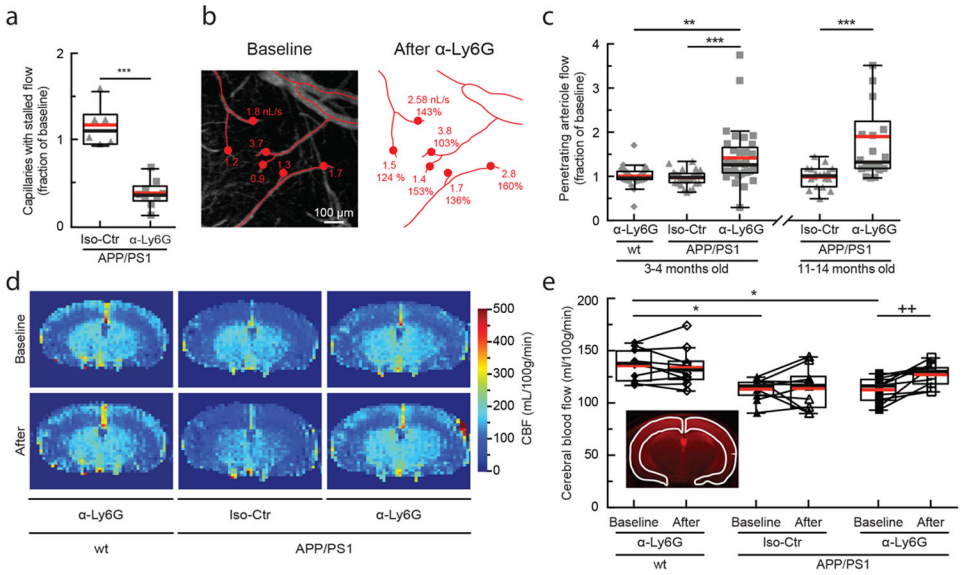

Fig. 3. Administration of antibodies against Ly6G reduced the number of stalled capillaries and increased cCBF in APP/PS1 mice.

(a) Number of capillaries with stalled blood flow ~1 hr after α-Ly6G or Iso-Ctr antibody administration (4 mg/kg animal weight, intraperitoneal) shown as a fraction of the number of stalled capillaries at baseline in APP/PS1 mice (α-Ly6G: n = 6 mice (3 female, 3 male), ~4,800 capillaries; Iso-Ctr: n = 6 mice (5 female, 1 male), ~4,800 capillaries; two-tailed Mann-Whitney, p=0.0004). (b) Projection of 2PEF image stack of brain surface vasculature, with surface (red lines) and penetrating (red dots) arterioles identified. For each penetrating arteriole, volumetric blood flow is indicated at baseline (left) and after α-Ly6G administration (right), along with the percentage of baseline flow. (c) Volumetric blood flow in penetrating arterioles measured 60-90 min after α-Ly6G or Iso-Ctr antibody administration in young and old APP/PS1 mice and wt control animals shown as a fraction of baseline arteriole flow (young APP/PS1 Iso-Ctr: n = 5 mice (1 female, 4 male), 32 arterioles; old APP/PS1 Iso-Ctr: n = 3 mice (1 female, 2 male), 18 arterioles; young wt α-Ly6G: n = 5 mice (3 female, 2 male), 30 arterioles; young APP/PS1 α-Ly6G: n = 5 (2 female, 3 male), 33 arterioles; old APP/PS1 α-Ly6G: n = 3 mice (all male), 22 arterioles; one-way Kruskal-Wallis ANOVA with post-hoc using Dunn's multiple comparison correction: young wt α-Ly6G vs. young APP/PS1 α-Ly6G p = 0.0023; young APP/PS1 Iso-Ctr vs. young APP/PS1 α-Ly6G p = 0.0000012; old APP/PS1 Iso-Ctr vs. old APP/PS1 α-Ly6G p = 0.00055). (d) CBF map measured using ASL-MRI at baseline and ~5 hr after administration of α-Ly6G or Iso-Ctr antibodies in APP/PS1 and wt mice. (e) cCBF measurements (ASL-MRI, inset indicates ROI on T2 MRI image) at baseline and ~5 hr after administration of α-Ly6G or Iso-Ctr antibodies in APP/PS1 and wt mice (wt α-Ly6G: n = 10 mice, APP/PS1 α-Ly6G: n = 10 mice, APP/PS1 Iso-Ctr: n = 10 mice; Ordinary one-way ANOVA with post hoc using Tukey's multiple comparison correction to compare across groups: baseline wt α-Ly6G vs. baseline APP/PS1 α-Ly6G p=0.011; baseline wt α-Ly6G vs. baseline APP/PS1 Iso-Ctr p=0.014; Paired t-test to compare baseline and after treatment within a group: baseline APP/PS1 α-Ly6G vs. after APP/PS1 α-Ly6G p=0.0058). All

boxplots are defined as: whiskers extend 1.5 times the difference between the value of the 75th and 25th percentile, median=black line and mean= red line.

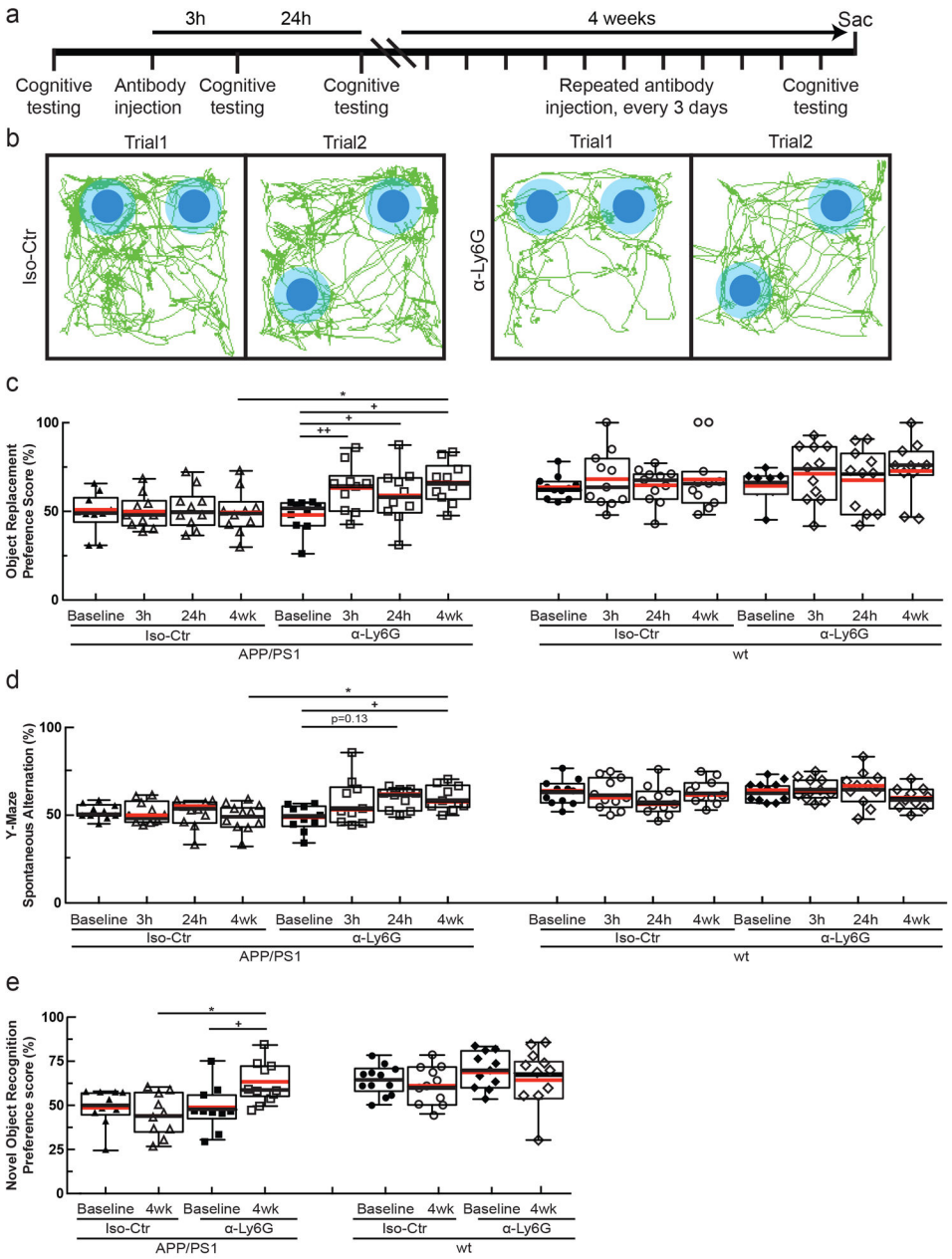

Fig. 4. Administration of α-Ly6G improved short-term memory.

(a) Experimental timeline for behavioral studies. (b) Tracking of mouse nose location from video recording during training and trial phases of OR task taken 3-5 hr after administration of α-Ly6G or Iso-Ctr antibodies in APP/PS1 mice (representative tracing maps). (c) Preference score in OR task and (d) spontaneous alternation in Y-maze task for APP/PS1 and wt mice at baseline and at 3 hr and 24 hr after a single administration of α-Ly6G or Iso-Ctr antibodies, and after 4 weeks of treatment every three days. (e) Preference score in NOR task for APP/PS1 and wt mice at baseline and after 4 weeks of treatment every three days. (APP/PS1 Iso-Ctr: n=10 mice (5 female, 5 female), APP/PS1 α-Ly6G: n=10 mice (5 female, 5 male), wt α-Ly6G: n=11 mice (7 female, 4 male), wt Iso-Ctr: n=11 mice (8 female, 3

male); one-way Kruskal-Wallis ANOVA with post-hoc using Dunn's multiple comparison correction to compare across groups: Object replacement APP/PS1 4wk Iso-Ctr vs. α-Ly6G p=0.029; Y-maze APP/PS1 4wk Iso-Ctr vs. α-Ly6G p=0.037; Novel object APP/PS1 4wk Iso-Ctr vs. α-Ly6G p=0.038; Friedman one-way repeated measures non-parametric ANOVA to compare baseline and after treatment results within a group: Object replacement APP/PS1 α-Ly6G baseline vs. 3 h p=0.0055, baseline vs. 24h p=0.016, baseline vs. 4wk p=0.045; Y-maze APP/PS1 α-Ly6G baseline vs. 24h p=0.13, baseline vs 4wk p=0.036; two-tailed Wilcoxon matched-pairs signed rank test to compare baseline and post-treatment with novel object APP/PS1 α-Ly6G baseline vs 4wk p=0.039.) All boxplots are defined as: whiskers extend 1.5 times the difference between the value of the 75th and 25th percentile, median=black line and mean= red line. All data in this figure represents the aggregation of two independently-conducted sets of behavioral experiments.

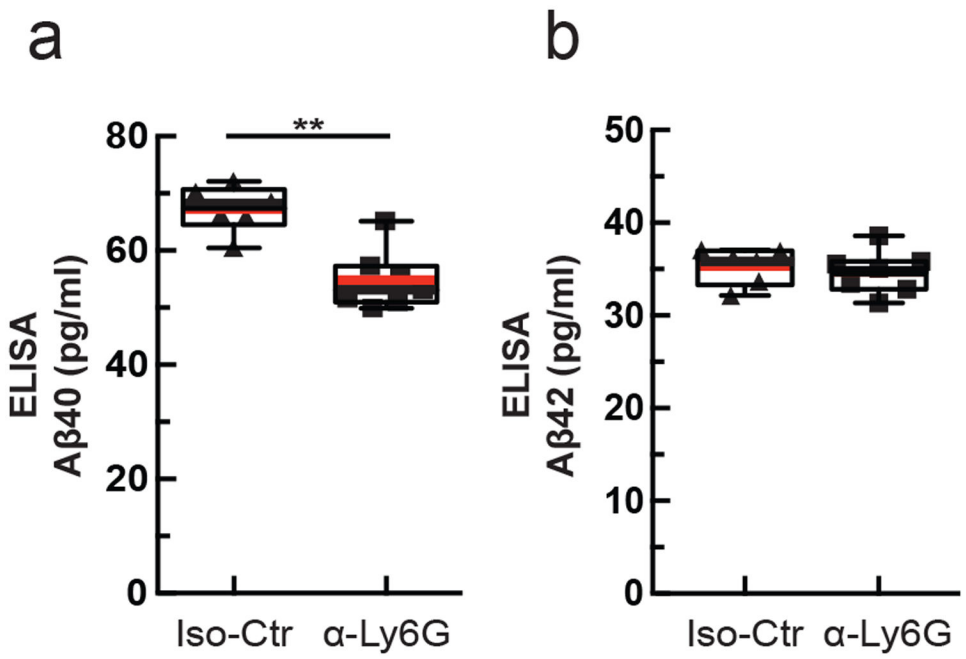

Fig. 5. Administration of α-Ly6G for one month decreased the concentration of Aβ1-40 in APP/PS1 mice.

ELISA measurements of (a) Aβ1-40 and (b) Aβ1-42 monomer concentrations after 4 weeks of treatment every three days (Iso-Ctr: n=6 mice (4 female, 2 male) and α-Ly6G: n=7 mice (4 female, 3 male); two-tailed Mann-Whitney p=0.0023). Boxplots are defined as: whiskers extend 1.5 times the difference between the value of the 75th and 25th percentile, median=black line and mean= red line.

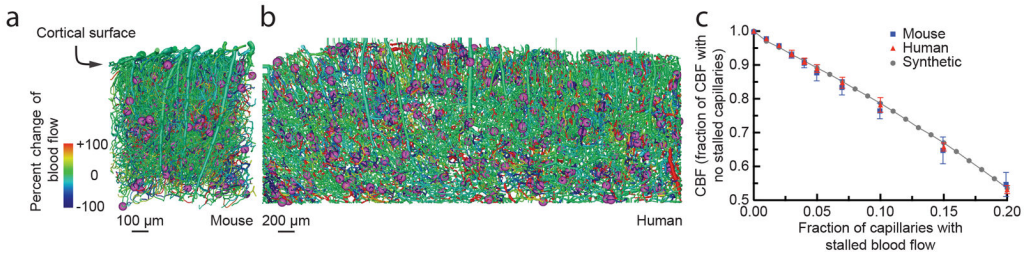

Fig. 6. Simulations predicted a similar CBF decrease in mouse and human cortical capillary networks with increasing fraction of capillaries with stalled flow.

Spatial maps of simulated blood flow changes caused by stalling of 2% of capillaries (indicated by purple spheres) in an mouse cortical vascular network (a, data on the structure and connectivity of murine cortical vascular network from [44]), and a human network (b, data on the structure and connectivity of human cortical vascular network from [22]). (c) Normalized cortical perfusion as a function of the fraction of capillaries that were occluded, expressed as a fraction of the perfusion with no occlusions, in mouse, human, and synthetic networks (data points represent the mean and error bars represent the SD across five independent simulations).